Particuology 115 (2026) 106–117

Contents lists available at ScienceDirect

Particuology

journal homepage: www.elsevier.com/locate/partic

Internal die flows of concentrated suspensions in slot coating processes considering shear-induced particle migration

Min-Kyu Kim[a], Hyun Wook Jung[a,b,*]

[a] Department of Battery-Smart Factory, Korea University, Seoul, 02841, Republic of Korea
[b] Department of Chemical and Biological Engineering, Korea University, Seoul, 02841, Republic of Korea

HIGHLIGHTS

- Shear-induced particle migration in concentrated suspensions markedly affects flow and particle distributions in slot dies.
- Particle nonuniformity at the feed inlet governs flow development in the chamber and slit.
- Particle distribution at the slit entrance controls widthwise advection and velocity profiles in the slit.
- Nonuniform inlet concentrations lead to exit-flow undulations and uneven wet thickness, including striped defects.

GRAPHICAL ABSTRACT

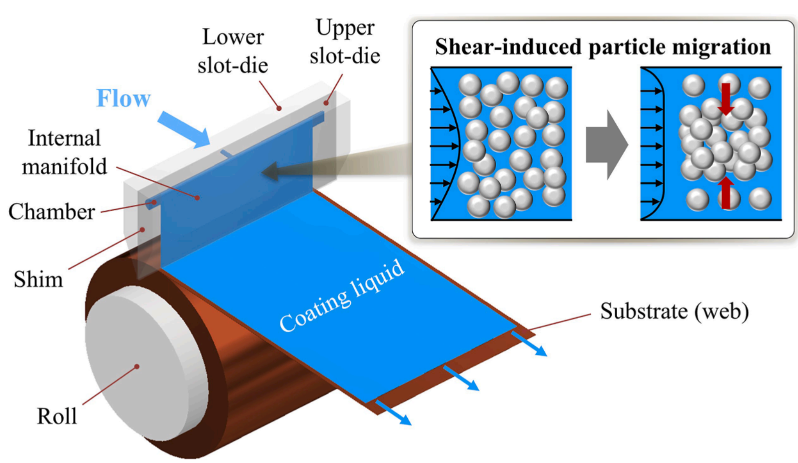

ARTICLE INFO

Keywords:
Slot coating
Internal die flow
Shear-induced particle migration
Concentrated suspension
Diffusive flux model

ABSTRACT

Shear-induced particle migration in the internal die flows of concentrated particulate suspensions during slot coating processes was investigated using a diffusive flux model implemented within three-dimensional computational fluid dynamics simulations. Comparative simulations demonstrated that particle migration markedly altered the internal flow characteristics and particle distributions inside the slot dies. Inhomogeneous particle distributions at the feed inlet were found to modify the flow behavior in the chamber region and profoundly affect the velocity and particle concentration fields in the slit region. These changes critically influenced the die exit velocity and concentration profiles, which governed the uniformity of the wet coating thickness. The insights obtained from this study offer practical guidance for die design and process control to achieve a uniform coating thickness and stable slot coating operation.

* Corresponding author. Department of Chemical and Biological Engineering, Korea University, Seoul, 02841, Republic of Korea.
E-mail address: hwjung@grtrkr.korea.ac.kr (H.W. Jung).

https://doi.org/10.1016/j.partic.2026.05.009
Received 17 February 2026; Received in revised form 4 May 2026; Accepted 12 May 2026
Available online 19 May 2026

1. Introduction

Slot coating is a pre-metered coating method in which the final wet film thickness is determined by operating conditions, such as the flow rate and web (or substrate) speed, rather than by the intrinsic material properties of the coating liquid. This feature enables the precise and reproducible control of the coating thickness, even under high-speed manufacturing conditions. Accordingly, slot coating has been widely adopted to produce functional films for various practical applications, including lithium-ion secondary batteries, solar cells, fuel cells, display panels, and flexible organic electronics (Ding et al., 2016; Kistler & Schweizer, 1997; Sartor, 1990; Schweizer, 2022).

Achieving stable and uniform deposition in slot coating critically depends on the flow dynamics within the coating bead region, which is a confined liquid bridge bounded by the die lips, the web, and the upstream and downstream menisci (Gates, 1999; Higgins & Scriven, 1980). Owing to the complexity of coating bead flows, extensive numerical and experimental studies have been conducted. For example, Higgins and Scriven (1980) developed a simplified viscocapillary model to predict the velocity and pressure fields in the coating bead region and identify the operability limits. Carvalho and Kheshgi (2000) further defined the low-flow limit as either the maximum attainable web speed at a given film thickness or the minimum achievable film thickness at a fixed web speed. Building on these foundational studies, various aspects of coating bead dynamics have been investigated, such as the effects of shear-thinning behavior (Koh et al., 2012; Park et al., 2022; Schmitt et al., 2013), viscoelasticity (Bajaj et al., 2008; Lee et al., 2017; Romero et al., 2004, 2006), viscoplasticity (Lee et al., 2023; Lee & Nam, 2016; Siqueira et al., 2024), tensioned-web-over-slot die configurations (Nam and Carvalho, 2010a, 2010b), multilayer coating (Ji et al., 2016; Nam and Carvalho, 2009, 2010c; Park et al., 2022), and porous substrates (Ding et al., 2013; Ding & Harris, 2017).

In addition to the bead flows, the internal die flows are closely linked to the coating bead dynamics and coating performance because the velocity distribution at the die exit directly influences both the coating bead dynamics and cross-web thickness uniformity. Accordingly, considerable effort has been devoted to predicting internal die flows and optimizing manifold designs. McKelvey and Ito (1971) and Matsubara (1979) proposed simplified models to describe the internal die flow characteristics of power-law fluids, whereas Leonard (1985) numerically analyzed the effects of inertia and gravity for various die geometries. Lee and Liu (1989) extended these analyses to dual-cavity coat-hanger dies. A comprehensive overview of slot-die design strategies was provided by Sartor (1990). More recently, three-dimensional computational fluid dynamics (CFD) studies have investigated the influence of shim configurations on the internal flows of shear-thinning fluids (Han et al., 2014; Jin et al., 2016), whereas data-driven and reduced-order modeling approaches, such as artificial neural networks (Kim et al., 2025) and surrogate models based on proper orthogonal decomposition (POD) (Ju et al., 2026), have been proposed to efficiently predict internal die flow characteristics.

However, in practical coating applications, coating liquids are often particulate suspensions rather than single-phase fluids. Concentrated slurries containing active materials, conductive agents, and polymeric binders are commonly employed in lithium-ion battery electrode fabrication. These suspensions exhibit pronounced non-Newtonian behavior arising from complex particle–particle and particle–fluid interactions. In this context, shear-induced particle migration has recently been recognized as an important phenomenon in slot coating for concentrated suspensions, as it can modify flow fields, alter particle distributions within the coated film, and affect operability limits and, ultimately, product performance (Campana et al., 2017; Kim & Jung, 2025; Rebouças et al., 2018; Siqueira & Carvalho, 2019; Siqueira et al., 2017).

Despite its importance, the direct experimental characterization of particle distributions in slot-coating flows remains extremely challenging. The confined microscale geometry of the slot die, combined with complex and often unsteady flow dynamics, severely limits optical access and in situ measurements. Consequently, the role of particle migration in slot coating, particularly its coupled influence on the internal die flows and coating bead dynamics, has not yet been fully elucidated. Min and Kim (2010) numerically investigated the velocity and particle concentration profiles in the coating bead region using a diffusive flux model (DFM), originally proposed by Phillips et al. (1992). The Carvalho group (Campana et al., 2017; Rebouças et al., 2018; Siqueira & Carvalho, 2019; Siqueira et al., 2017) extensively examined the particle migration and low-flow limits in various suspension slot coating systems using finite element simulations incorporating the DFM. More recently, Kim and Jung (2025) analyzed the effects of particle migration on coating bead dynamics and operability windows using a finite-volume framework incorporating the DFM, and further identified a novel mechanism underlying periodic particle concentration oscillations driven by flow–concentration coupling within the coating bead region during slot coating in the low capillary number regime (Kim & Jung, 2026).

In contrast to previous studies that focused on particle migration in coating bead flows, the migration phenomena within internal die flows have received far less attention. In industrial-scale battery manufacturing, the feed pipeline upstream of the slot die is often sufficiently long for the suspension flow to fully develop before entering the die, which can lead to inherently nonuniform particle distributions at the feed inlet. Therefore, controlling the inlet particle distribution is crucial because the inlet conditions can markedly reshape the internal die flows and, in turn, affect the coating bead dynamics downstream. Generally, storage tanks are equipped with agitation systems to prevent particle settling and maintain homogeneous suspensions. However, when mixing is insufficient or absent, the resulting effects on the subsequent coating process have not yet been fully elucidated. This highlights the need for a quantitative assessment of how inlet concentration nonuniformity affects the internal die flow characteristics, which govern the velocity and particle concentration profiles at the die exit and ultimately dictate the coating bead dynamics and overall process stability.

In this study, we investigated the shear-induced particle migration in the internal die flows of concentrated suspensions during slot coating using three-dimensional CFD simulations incorporating the DFM. The coating liquid was modeled as a suspension of spherical particles dispersed in a Newtonian medium, providing a simplified yet representative framework for examining the particle migration effects. Comparative simulations of the internal die flows revealed that particle migration substantially alters the flow fields within the die manifold and critically affects the uniformity of the velocity and particle concentration at the die exit. Furthermore, the effects of inhomogeneous particle distributions generated at the feed inlet through long-supply pipelines were systematically evaluated, and the distinct behaviors of particulate suspensions were compared with those of fluids without particles, that is, Newtonian and shear-thinning fluids.

2. Governing equations and simulation methods

Fig. 1(a) and (b) schematically illustrate the slot coating flow and slot-die structure, respectively. One or more shims are inserted between the upper and lower slot dies to define the manifold geometry, which consists of a chamber and slit region. After entering the feed inlet, the coating liquid is redistributed in the cross-web (widthwise) direction within the chamber and subsequently passes through the narrow slit. Upon exiting the slot-die lips, the liquid is deposited onto the moving web, forming a coating bead.

Fig. 1(c) shows the manifold configuration of the internal die flows examined in this study. Here, R_f and L_f denote the radius and length of the feed inlet, respectively; R_c and W_c are the radius and width of the chamber, respectively; and L_s, W_s, and H_s represent the length, width, and height of the slit region, respectively. The dimensions of the internal manifold summarized in Table 1 correspond to the typical geometry adopted in a previous study (Jin et al., 2016). The origin was defined as

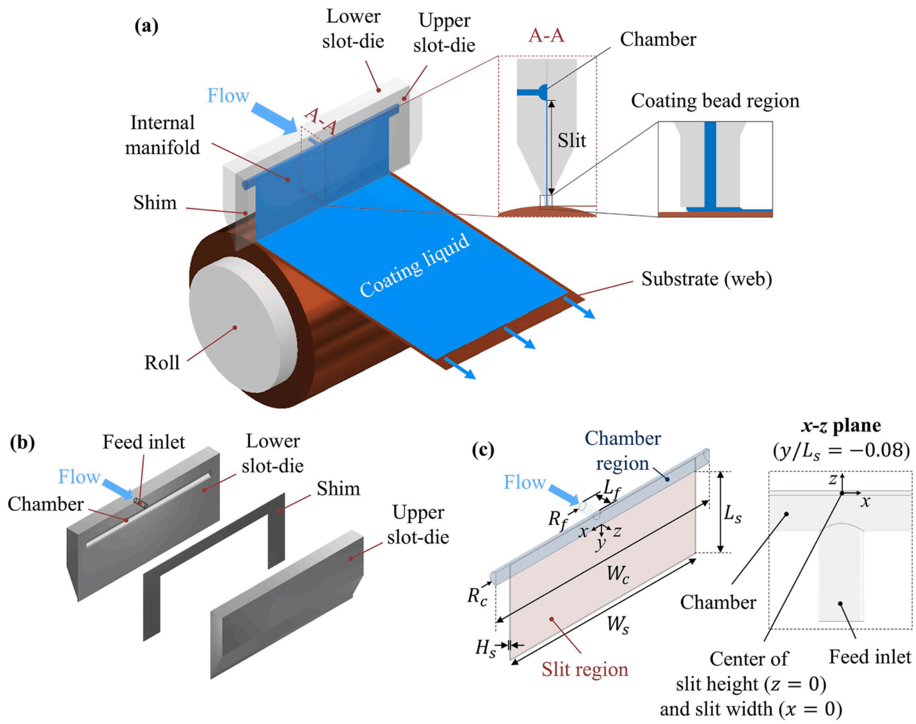

Fig. 1. Schematics of (a) the slot coating flow, (b) slot-die structure, and (c) internal flow geometry consisting of both the chamber and slit regions, respectively.

the center of the slit width ($x = 0$) and slit height ($z = 0$) at the entrance of the slit region ($y = 0$), as illustrated in Fig. 1(c).

The internal die flows of particulate suspensions consisting of non-colloidal, non-Brownian, monodisperse, and neutrally buoyant hard spheres dispersed in a Newtonian solvent are governed by the following equations:

$$\textit{Equation of continuity (EOC)} : \underline{\nabla}\cdot\underline{v} = 0 \tag{1}$$

$$\textit{Equation of motion (EOM)} : \rho\left(\frac{\partial \underline{v}}{\partial t} + \underline{v}\cdot\underline{\nabla}\underline{v}\right) = -\underline{\nabla}P + \underline{\nabla}\cdot\underline{\underline{\tau}} \tag{2}$$

$$\textit{Diffusive flux model (DFM)} : \frac{\partial \phi}{\partial t} + \underline{v}\cdot\underline{\nabla}\phi = -\underline{\nabla}\cdot[\underline{N}_c + \underline{N}_\eta] \tag{3}$$

Table 1
Summary of slot-die design parameters and simulation conditions.

Parameter	Value
a Particle radius, μm	10
c Exponent of the Krieger model	1.82
H_s Height of the slit region (or feed slot gap), mm	0.5
K_c Parameter for the collision frequency gradient term	0.41
K_η Parameter for the viscosity gradient term	0.62
L_f Length of the feed inlet, mm	10
L_s Length of the slit region, mm	50
n_C Power-law index in the Carreau model	0.4
P_a Ambient pressure, Pa	101325
Q_i Inlet volumetric flow rate, cm^3/s	3.64
R_c Radius of the chamber, mm	4
R_f Radius of the feed inlet, mm	2.5
W_c Width of the chamber, mm	150
W_s Width of the slit region, mm	130
η_s Viscosity of the solvent, Pa s	2.0×10^{-3}
η_0 Zero-shear viscosity in the Carreau model, Pa s	3.5
η_∞ Infinite-shear viscosity in the Carreau model, Pa s	0.003
λ_C Relaxation time in the Carreau model, s	35
ρ Density of the coating liquid, kg/m^3	1210
ρ_p Density of the particle, kg/m^3	1210
ϕ_0 Average bulk particle volume fraction	0.5
ϕ_m Maximum packing volume fraction	0.68

where $\underline{v}$ represents the velocity vector, t is the time, ρ is the density, P is the pressure, $\underline{\underline{\tau}}$ is the viscous stress tensor, and ϕ denotes the particle volume fraction. To capture shear-induced particle migration, two representative models are widely used: (1) the diffusive flux model (DFM) (Phillips et al., 1992) and (2) the suspension balance model (SBM) (Nott & Brady, 1994). The DFM describes shear-induced particle migration as a balance between particle fluxes driven by gradients in collision frequency and suspension viscosity. In contrast, the SBM attributes shear-induced particle migration to the normal stresses in the suspension and treats it as a two-phase system consisting of a suspending fluid and a dispersed particle phase. Hampton et al. (1997) demonstrated that the DFM provides more reliable predictions for moderate concentration ranges (20–45 vol %) and relatively small particle sizes (particle-to-channel radius ratio of approximately 0.02). Based on these considerations, the DFM is employed in this study. The two particle fluxes in the DFM (Eq. (3)), namely the collision frequency gradient term and the viscosity gradient term, are expressed as follows:

$$\textit{Collision frequency gradient term} : \underline{N}_c = -K_c a^2 \phi \underline{\nabla}(\phi\dot{\gamma}) \tag{4}$$

$$\textit{Viscosity gradient term} : \underline{N}_\eta = -K_\eta a^2 \dot{\gamma}\phi^2 \underline{\nabla}\ln\eta \tag{5}$$

where $K_c = 0.41$ and $K_\eta = 0.62$ are empirical parameters (Kim & Jung, 2025; Min & Kim, 2010; Nott & Brady, 1994; Phillips et al., 1992); a is the particle radius; $\dot{\gamma} = \sqrt{2\underline{\underline{D}}:\underline{\underline{D}}}$ is the magnitude of the shear rate; $\underline{\underline{D}} = 0.5(\underline{\nabla}\underline{v} + \underline{\nabla}\underline{v}^T)$ is the rate-of-deformation tensor; and η is the suspension viscosity. Shear-induced particle migration leads to local variations in ϕ and, consequently, to spatial variations in η.

The stress tensor was modeled using a generalized Newtonian fluid formulation with a concentration-dependent viscosity model proposed by Krieger (1972),

$$\underline{\underline{\tau}} = 2\eta(\phi)\underline{\underline{D}} = 2\eta_s\left(1 - \frac{\phi}{\phi_m}\right)^{-c}\underline{\underline{D}} \tag{6}$$

where η_s is the viscosity of the Newtonian solvent, $c = 1.82$ is the exponent of the viscosity model, and $\phi_m = 0.68$ is the maximum packing volume fraction for hard spheres (Chun et al., 2017; Krieger, 1972; Phillips et al., 1992).

The governing equations (Eqs. (1)–(3)) are subject to the following boundary conditions (BCs):

Wall BCs :

$$\underline{v} = \underline{0} : \text{no slip} \tag{7}$$

$$\underline{n} \cdot \left(K_c a^2 \phi \underline{\nabla}(\phi \dot{\gamma}) + K_\eta \dot{\gamma} \phi^2 \left(\frac{a^2}{\eta} \right) \underline{\nabla} \eta \right) = 0 : \text{no particle flux} \tag{8}$$

Inlet BCs :

$$Q = Q_i : \text{constant volumetric flow rate} \tag{9}$$

$$\phi = \phi_0 : \text{uniform } \phi \text{ distribution} \tag{10a}$$

$$\frac{\phi_w}{\phi} \left(\frac{\phi_m - \phi}{\phi_m - \phi_w} \right)^{-c(1 - K_\eta / K_c)} = |r^*| : \text{fully developed } \phi \text{ distribution} \tag{10b}$$

Outlet BCs :

$$P = P_a : \text{ambient pressure} \tag{11}$$

$$\underline{n} \cdot \underline{\nabla} \phi = 0 : \text{zero} - \text{gradient particle concentration} \tag{12}$$

where $\underline{n}$ is the unit normal vector to the boundary, Q_i is the inlet volumetric flow rate, ϕ_0 is the average bulk particle volume fraction, subscript w denotes the wall, and $r^* = r/R_f$ is the normalized radial position at the feed inlet.

To investigate the effect of the initial particle distribution at the feed inlet, two types of inlet BCs were considered: (1) a uniform ϕ BC (Eq. (10a)) and (2) a fully developed ϕ BC (Eq. (10b)). Equation (10b) was implemented using the semi-analytic solution outlined by Phillips et al. (1992), which predicted the radial distribution of the particle volume fraction at the inlet. The inlet BCs were designed to represent realistic conditions in practical feed systems. Eq. (10a) corresponds to a well-controlled, uniform particle distribution that may occur under effective mixing in the storage tank and a short supply pipeline connecting the tank to the coater. In contrast, Eq. (10b) represents a parabolic particle distribution that can arise from insufficient mixing or transport through a long feed pipeline, where shear-induced migration becomes significant. The initial conditions for the velocity, pressure, and particle concentration fields were specified using the steady-state solution obtained under a uniform particle concentration, that is, $\phi = \phi_0$ in the coating liquid.

Simulations were performed using a finite volume method-based CFD solver (ANSYS FLUENT, v17.0), coupled with an in-house code developed to solve the DFM (Eq. (3)). The resolution of the computational mesh representing the internal die manifold was carefully determined through a mesh convergence test (see Appendix), optimizing the trade-off between numerical accuracy and computational cost. The total number of meshes was 9,529,747 elements to ensure reliable numerical solutions, with finer meshes densely distributed in the slit region (22 elements in the z-direction across the feed slot gap). Transient simulations were conducted using a time step of 5×10^{-4} s, which was carefully determined based on slit-flow simulations reported in our previous work (Kim & Jung, 2025). The semi-implicit method for pressure-linked equations consistent (SIMPLEC) scheme was employed for pressure–velocity coupling. The pressure staggering option (PRESTO) and the third-order monotonic upstream-centered (MUSCL) scheme were used for the discretization of pressure and momentum, respectively. This CFD framework incorporating the DFM was validated in our previous study (Kim & Jung, 2025, 2026).

3. Results and discussion

To clarify how particle migration and different initial particle distributions influence the internal die flow dynamics, simulations of particulate suspensions were compared with those of pure Newtonian and shear-thinning fluids. In particular, suspension cases with distinct particle concentration profiles prescribed at the feed inlet were considered, as described in Section 2. The simulation cases are defined as follows:

(1) Case S-U: suspension with a uniform ϕ profile at the feed inlet (Eq. (10a));
(2) Case S-F: suspension with a fully developed ϕ profile at the feed inlet (Eq. (10b));
(3) Case N: pure Newtonian fluid without particles;
(4) Case C: Carreau-type shear-thinning fluid without particles.

The detailed slot-die design parameters and simulation conditions are summarized in Table 1. Given the geometric complexity of the internal die manifold, a schematic indicating the corresponding observation location is included in each figure in this section.

3.1. Internal die flows of generalized Newtonian fluids without particles

For comparison, pure Newtonian and Carreau-type shear-thinning coating liquids without particles were simulated. The Carreau-type shear viscosity is expressed as follows:

$$\eta = \eta_\infty + (\eta_0 - \eta_\infty)\left(1 + (\lambda_C \dot{\gamma})^2\right)^{(n_C - 1)/2} \tag{13}$$

where η_∞, η_0, λ_C, and n_C represent the infinite-shear viscosity, zero-shear viscosity, characteristic time constant, and power-law index of the Carreau model, respectively. Here, the Newtonian viscosity in case N was set to be equal to the suspension viscosity evaluated at $\phi = \phi_0$, and the viscosity-related parameters in case C were adopted from a previous study (Jin et al., 2016), where they were obtained by fitting experimental shear viscosity data for a xanthan gum polymer solution.

Fig. 2 compares the velocity fields inside the slit region for two generalized Newtonian fluid cases without particles (cases N and C), including contours with streamlines of v^* in the slit region at the center of the slit height ($z = 0$) (Fig. 2(a)), as well as v^* profiles along the slit width (Fig. 2(b)) and along the slit height (Fig. 2(c)) at the die exit.

As shown in Fig. 2(a) and (b), case N exhibited highly uniform velocity distributions in the widthwise (x) direction at the die exit, which is a desirable condition for a stable and defect-free coating. In contrast, case C displayed nonuniform parabolic velocity profiles across the slit width direction owing to the shear-thinning effect. As reported in previous studies (Jin et al., 2016), the velocity near the center of the slit width ($x = 0$) at the die exit increases for shear-thinning fluids because the effective shear rate decreases from the middle to the edges across the slit width in the chamber-to-slit transition region, thereby reducing the effective shear viscosity near the center of the slit width and inducing slightly parabolic velocity profiles.

Fig. 2(c) further illustrates that case C displays a noticeably blunter velocity profile along the slit height at the die exit compared with case N, which is characteristics of shear-thinning behavior.

3.2. Internal die flows of particulate suspensions

3.2.1. Particle concentration and velocity distributions within internal die manifold

The suspension cases (S-U and S-F) exhibited complex internal die flow features arising from shear-induced particle migration, in contrast to the generalized Newtonian cases (cases N and C) (see Appendix), which did not contain particles. Figs. 3 and 4 show the contours of the particle volume fraction (ϕ) and normalized velocity magnitude ($v^* = |\underline{v}| W_s H_s / Q_i$) at the midplane cross-sections of the chamber and feed inlet at $y/L_s = -0.08$ and $x = 0$, respectively, for the suspension cases. As shown in Fig. 3(a), case S-U exhibits a homogeneous particle distribution throughout the chamber, whereas case S-F displays a highly

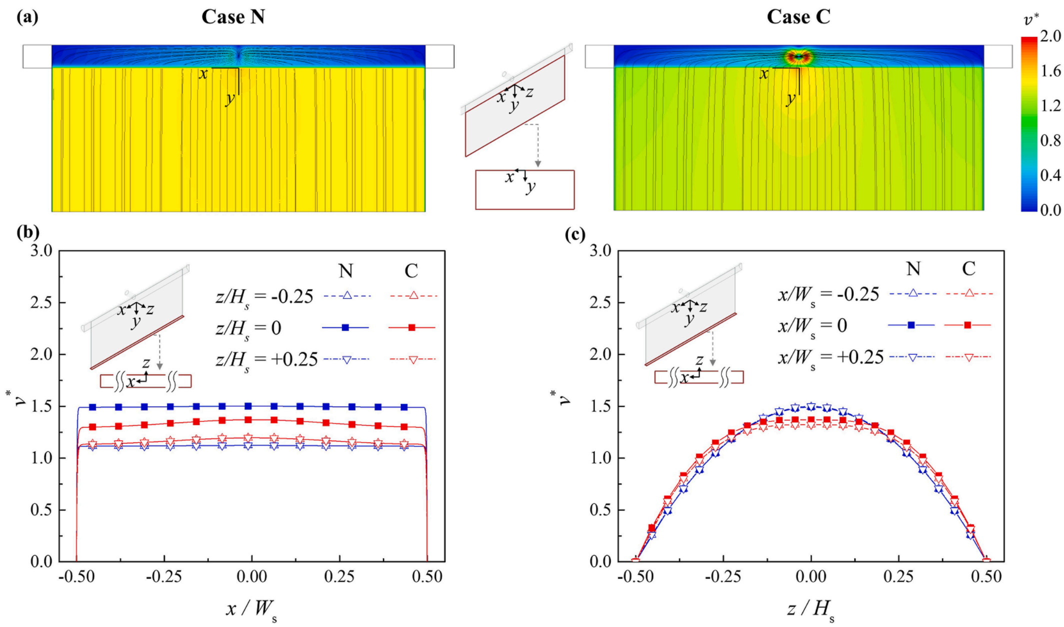

Fig. 2. Comparisons between the Newtonian fluid (case N) and Carreau-type shear-thinning fluid (case C); (a) normalized velocity magnitude contour at $z = 0$ in the slit region; (b, c) normalized velocity profiles at the die exit in the widthwise (x) and gapwise (z) directions. Carreau model parameters: $\eta_0 = 3.5$ Pa· s, $\eta_\infty = 0.003$ Pa·s, $\lambda_C = 35$ s, and $n_C = 0.4$.

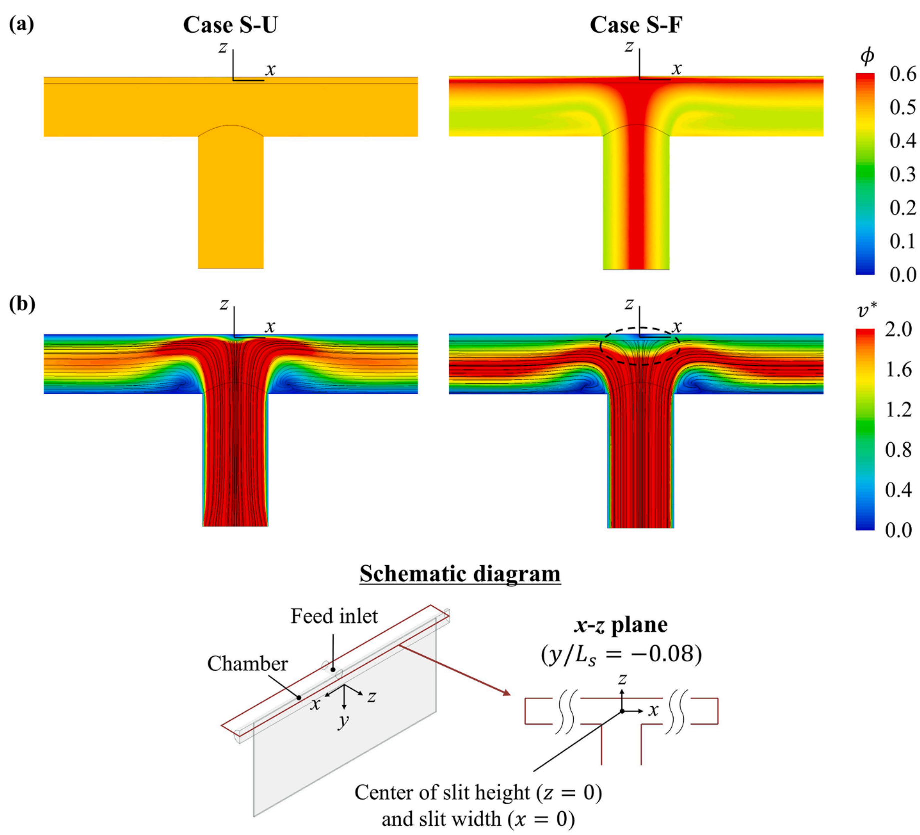

Fig. 3. (a) Particle volume fraction and (b) normalized velocity magnitude contours at the middle cross-section of the chamber and feed inlet ($y/L_s = -0.08$) for the suspension cases.

inhomogeneous distribution. In case S-F, the particles concentrated along the feed inlet centerline ($x = 0$) were transported directly toward the slit center and remained insufficiently redistributed within the chamber. This dense particle accumulation near the bifurcation region of the feed inlet centerline in case S-F suppressed the local velocity and caused the flow to deviate laterally relative to that in case S-U, as illustrated in Fig. 3(b).

Fig. 4(a–d) show consistent trends in particle concentration and

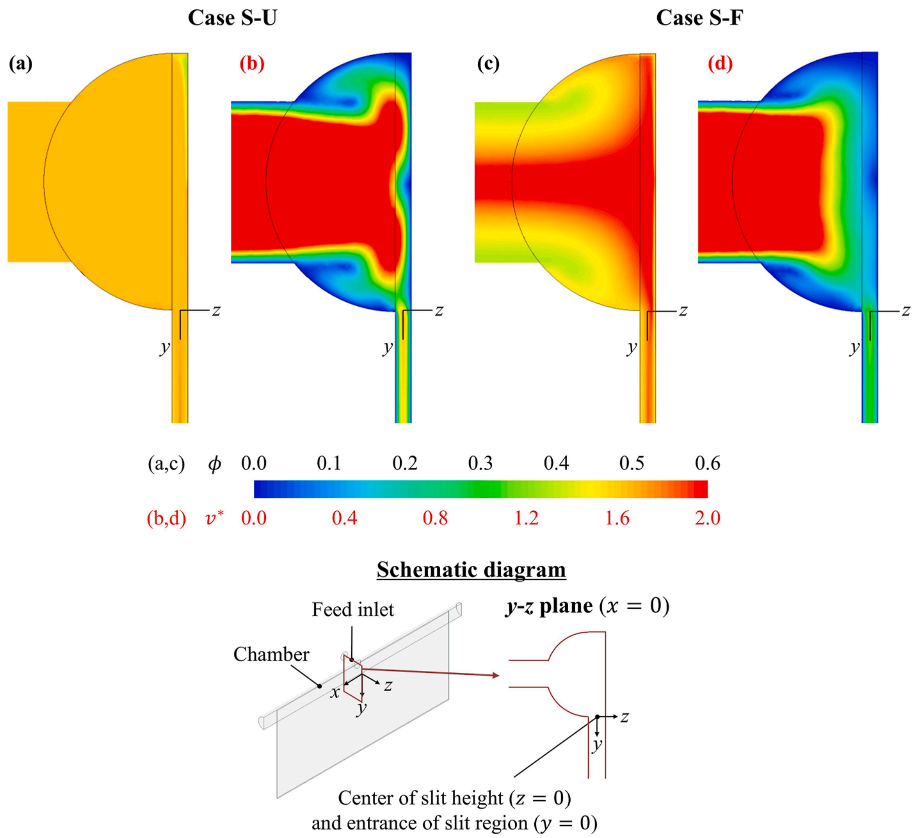

Fig. 4. (a, c) Particle volume fraction and (b, d) normalized velocity magnitude contours at the middle cross-section of the chamber and feed inlet ($x = 0$) for the suspension cases.

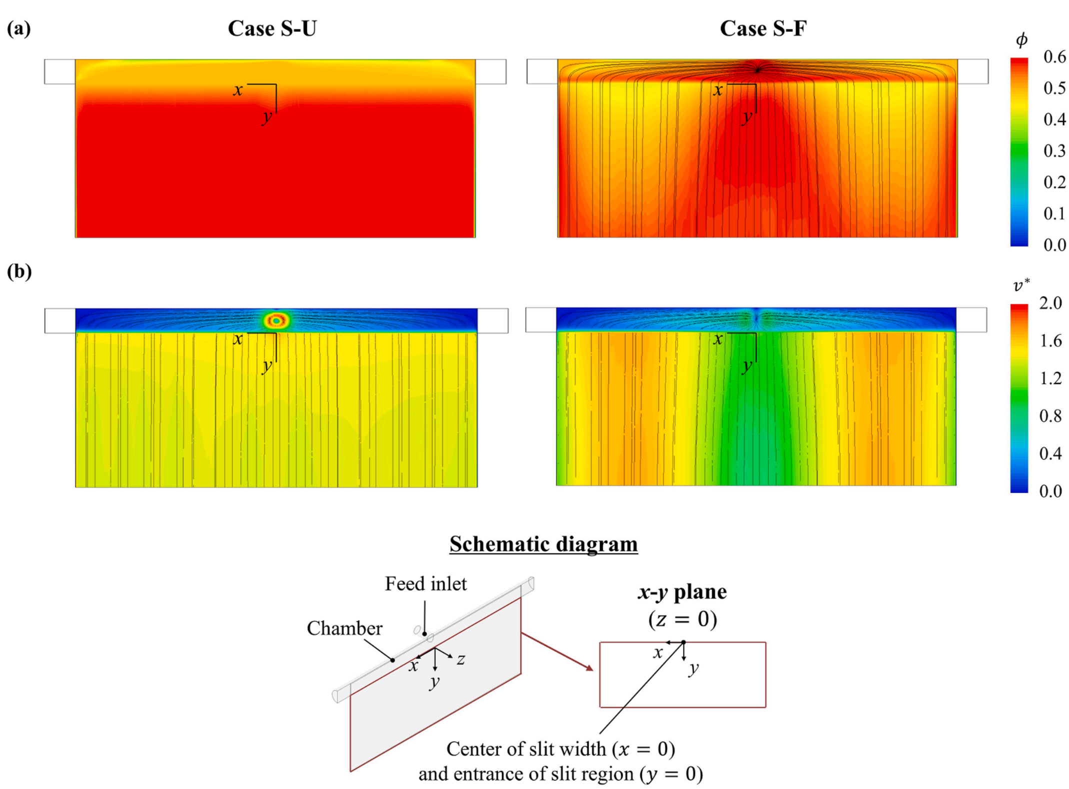

Fig. 5. Contours of (a) particle volume fraction and (b) normalized velocity magnitude at the center of the slit height ($z = 0$) in the slit region for the suspension cases.

velocity fields in the y-z plane cross-section of the chamber region, further confirming that the particle concentration patterns and associated flow distortions observed in Fig. 3 are three-dimensional in nature. In Fig. 4(a), case S-U maintained a nearly uniform particle distribution throughout the chamber, whereas case S-F exhibited a pronouncedly inhomogeneous particle distribution. Notably, in Fig. 4(c), the dense particle concentration along the feed inlet centerline ($y/L_s = -0.08$) was advected upward along curved streamlines near the slit entrance and formed a concentration peak at $z > 0$. Fig. 4(b) and (d) show distinct differences in flow characteristics in the transition region from the chamber to the slit between cases S-U and S-F, and further support that the normalized velocity at the center of the slit entrance is locally suppressed due to the dense particle accumulation near the bifurcation region, as displayed in Fig. 3(b). These flow dynamics within the chamber ultimately govern the flow and particle concentration fields in the subsequent slit region and consequently affect the resulting ϕ and v^* profiles at the die exit.

Fig. 5(a) and (b) show ϕ and v^* contours at the center of the slit height ($z = 0$) in the slit region for the suspension cases, respectively. In Fig. 5(a), the widthwise ϕ profile of case S-U at the center of the slit height ($z = 0$) quickly approaches ϕ_m along the slit length, indicating migration-driven centerline packing across the slit height in the narrow-gap flow. This behavior arises because shear-induced particle migration transports particles from high-shear regions near the slit walls toward the low-shear region near the centerline. In addition, case S-U exhibits an almost uniform particle distribution across the slit width, facilitated by the large aspect ratio of the slit channel. In contrast, case S-F reveals pronounced concentration inhomogeneity resulting from the nonuniform feed-inlet condition. The widthwise ϕ profile of case S-F at $z = 0$ gradually approaches ϕ_m along the slit length; however, noticeable widthwise variations persist, indicating that particle migration in the widthwise direction is insufficient to achieve a fully-developed state under the given conditions in case S-F.

Fig. 5(b) shows that v^* is nearly uniform along the width for case S-U, similar to case N, whereas case S-F exhibits strong velocity nonuniformity. This deviation originated from a locally dense particle region near the center of the slit entrance, where the centerline velocity was significantly suppressed owing to the locally elevated viscosity. These results indicate that the homogenization of the particle concentration within the chamber is insufficient when a fully developed particle concentration profile is supplied at the feed inlet, ultimately leading to the distortion of the velocity field as the flow enters the slit, which is consistent with the chamber-scale dynamics discussed in Figs. 3 and 4.

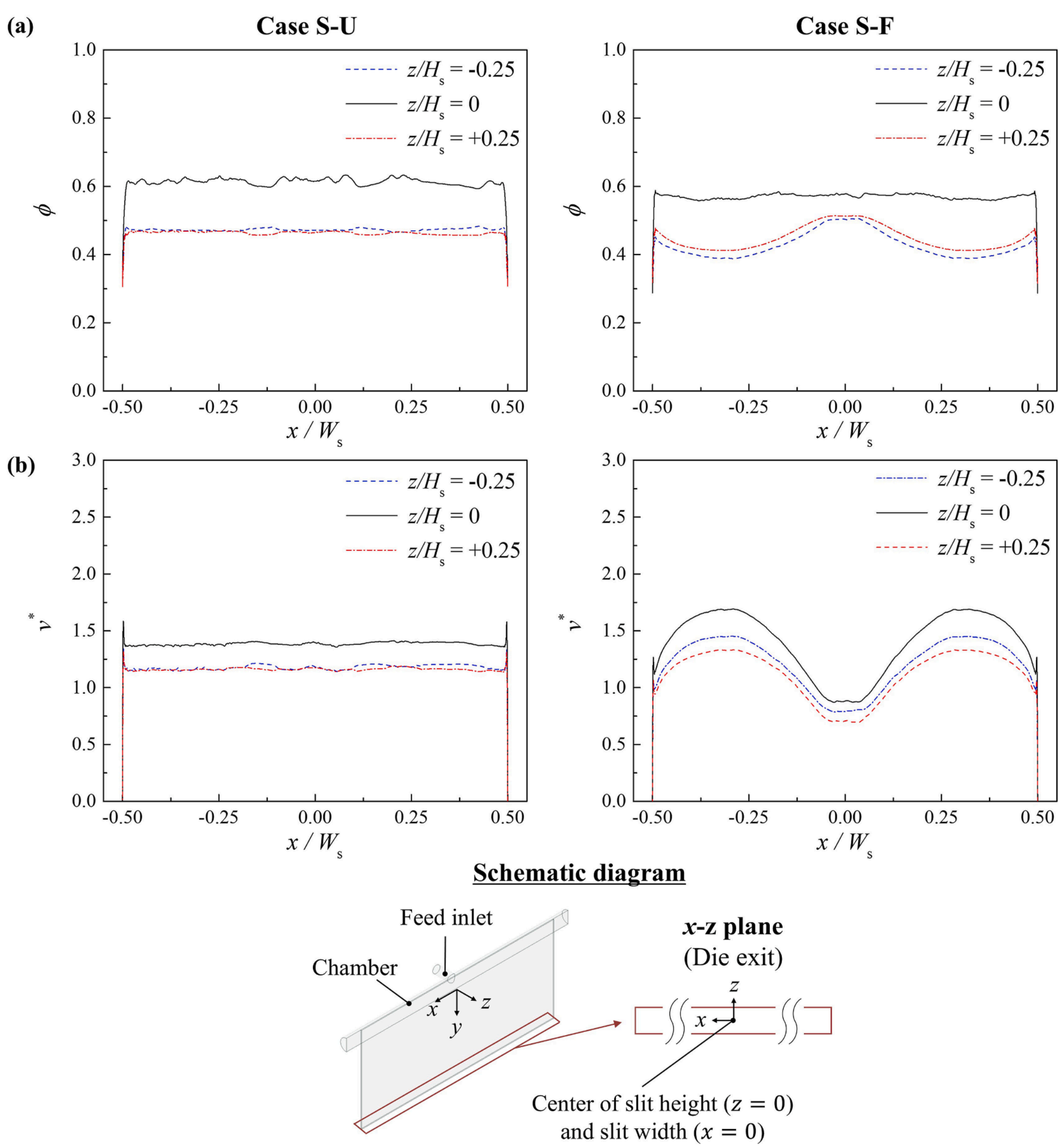

Fig. 6. Widthwise profiles of (a) particle volume fraction and (b) normalized velocity magnitude at various z-positions at the die exit for the suspension cases.

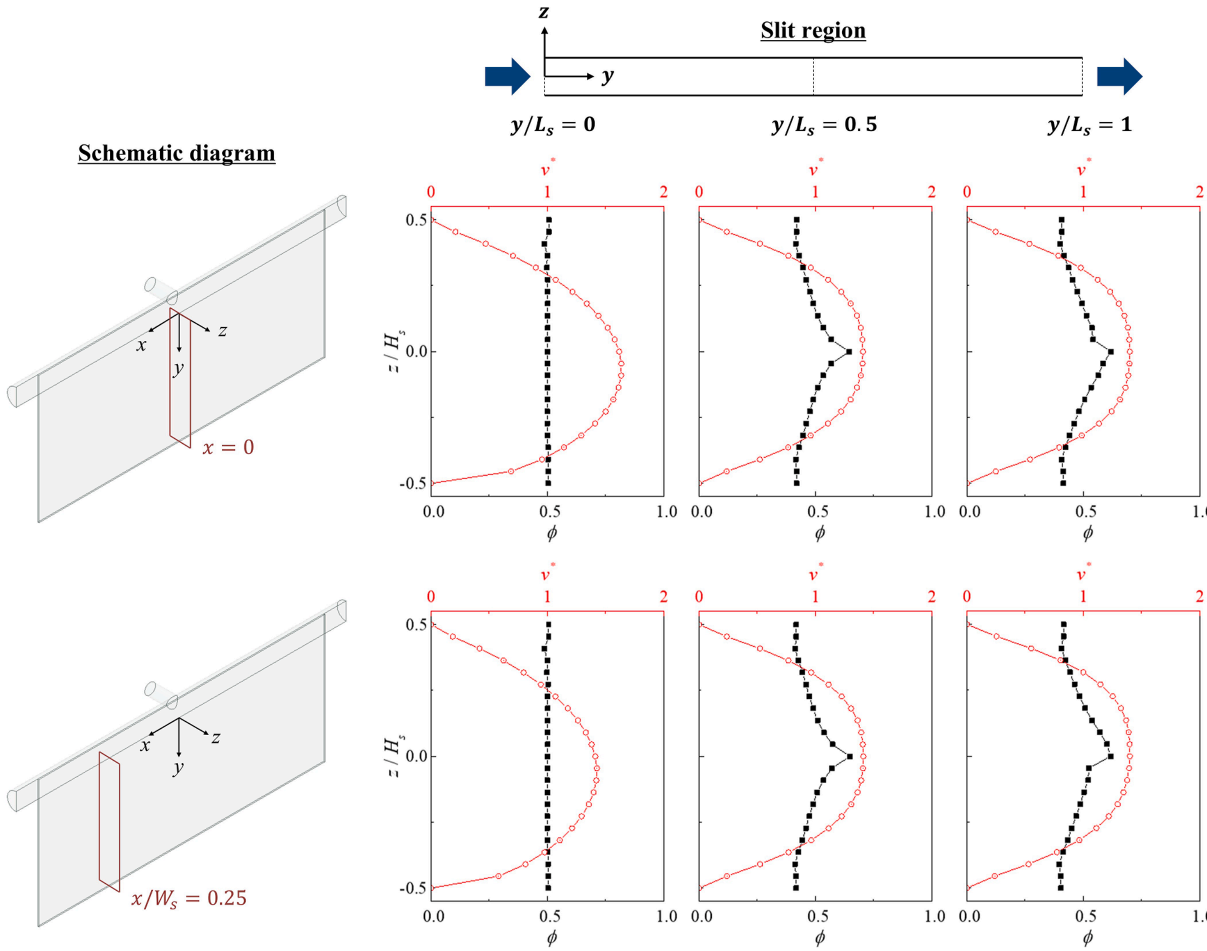

Fig. 7. Evolution of the particle concentration and normalized velocity magnitude across the slit height at various *y*-positions ($y/L_s = 0, 0.5, 1$) in the slit region for case S-U.

Fig. 6(a) and (b) show the widthwise ϕ and v^* profiles at different *z*-positions of the die exit for the suspension cases. In case S-U, the particle concentration was evenly distributed, and favorable uniformity of the widthwise velocity profiles was obtained. However, gapwise variations in ϕ were observed, resulting from shear-induced migration in the narrow-slit gap region. Previous studies have shown the development length (L_{dev}) for shear-induced migration scales with the cube of a characteristic length (l_c), that is $L_{dev} \sim \left(l_c^3/a^2\right)$ (Kwon et al., 2018; Nott & Brady, 1994). Here, l_c corresponds to the slit dimension, either the gap height H_s or the slit width W_s. As a result, migration in the gapwise direction develops much more rapidly because H_s is significantly smaller than W_s, whereas widthwise migration remains comparatively weak. Consistent with case S-U, case S-F also exhibits gapwise variations in ϕ, as shown in Fig. 6(a). The widthwise ϕ profile at $z = 0$ becomes uniform and approaches ϕ_m because of the shear-induced migration, whereas those at $z/H_s = \pm 0.25$ display axisymmetric concave curvatures toward the centerline ($x = 0$). These particle concentration distributions lead to convex velocity profiles (Fig. 6(b)).

3.2.2. Evolution of particle concentration and velocity profiles

Figs. 7 and 8 show the evolution of ϕ and v^* across the slit height at various *y*-positions in the slit region for cases S-U and S-F, respectively. In Fig. 7, for case S-U, the particle distributions at the entrance of the slit region were uniform. After entering the slit region, the ϕ profiles were nearly symmetric with a centerline peak ($z = 0$), and those at different *x*-positions were nearly identical. In addition, case S-U exhibited blunt gapwise v^* profiles in the slit region owing to the centerline peak in the ϕ. These observations indicate that the gapwise ϕ and v^* profiles reflect the characteristic behavior of the planar Poiseuille flow in concentrated particulate suspensions, whereas the widthwise ϕ distribution remains uniform within the slit channel. Throughout the slit region, case S-U approached a fully developed state at the die exit.

In contrast, as shown in Fig. 8, case S-F exhibited *x*-position-dependent profiles for both ϕ and v^* throughout the slit region. In particular, v^* at $x = 0$ was significantly lower than that at $x/W_s = 0.25$ because of the locally elevated particle concentration and the consequent increase in the suspension viscosity near the center of the slit entrance. Case S-F also displayed pronounced widthwise variations in both ϕ and v^* at the die exit. These observations indicate that shear-induced particle migration in case S-F in the widthwise direction is insufficient to approach a fully developed state, which is consistent with the discussion of Fig. 6.

3.2.3. Widthwise advection in slit region

The widthwise particle advection in the slit region is also influenced by the particle distributions established within the chamber. Fig. 9(a) and (b) show the normalized *x*-velocity magnitude, $v_x^* = v_x W_s H_s / Q_i$, along the slit width at different *y* positions for the suspension cases at the center of the slit height ($z = 0$). In case S-U (Fig. 9(a)), v_x^* decreased drastically along the slit length and approached zero. In contrast, in case S-F (Fig. 9(b)), the maximum value of v_x^* near the center of the slit entrance was noticeably lower than that in case S-U owing to the locally dense particle concentration, as shown in Fig. 5(a). Furthermore, the persistence of the nonzero v_x^* at the die exit in case S-F indicates ongoing widthwise advection and an underdeveloped flow over the given slit length,

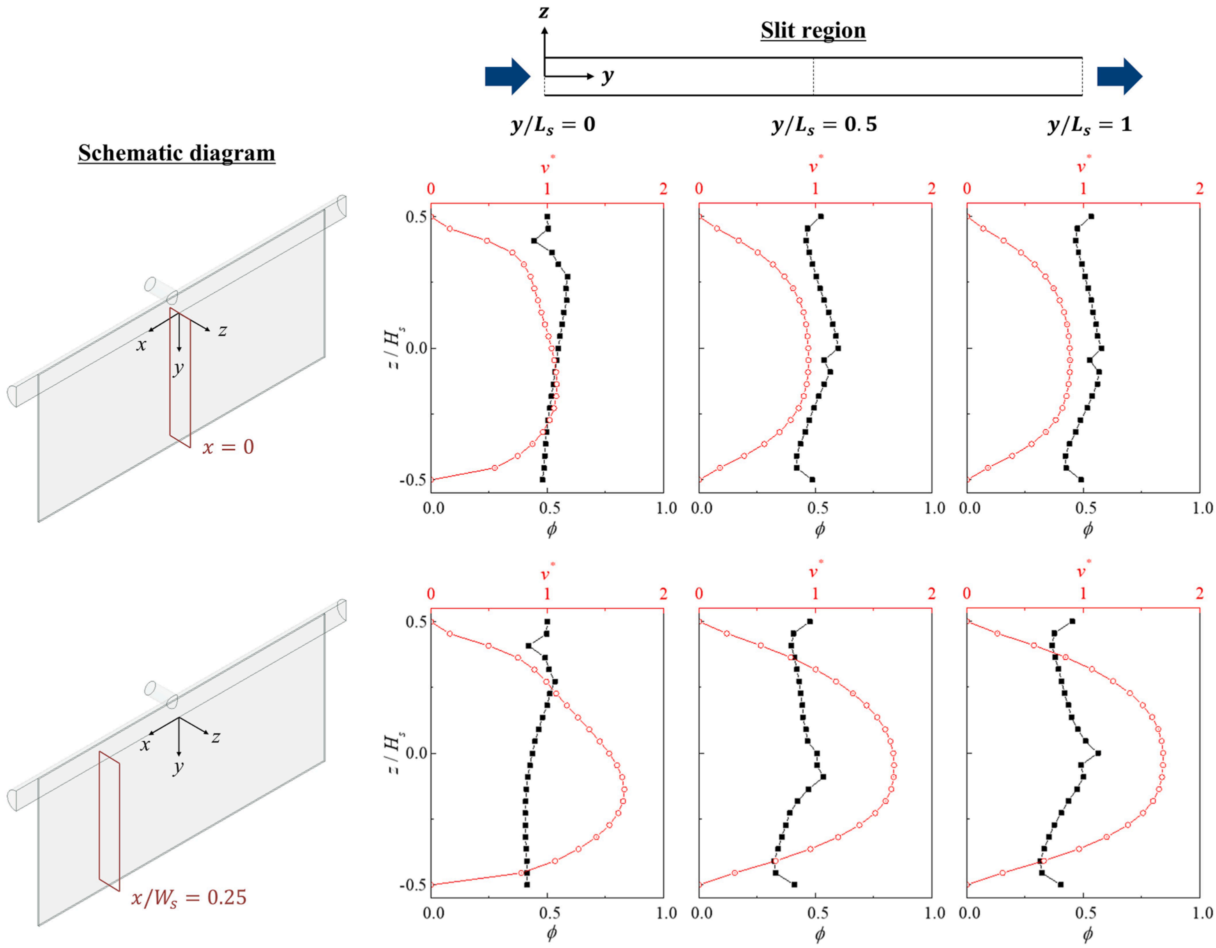

Fig. 8. Evolution of the particle concentration and normalized velocity magnitude across the slit height at various y-positions ($y/L_s = 0, 0.5, 1$) in the slit region for case S-F.

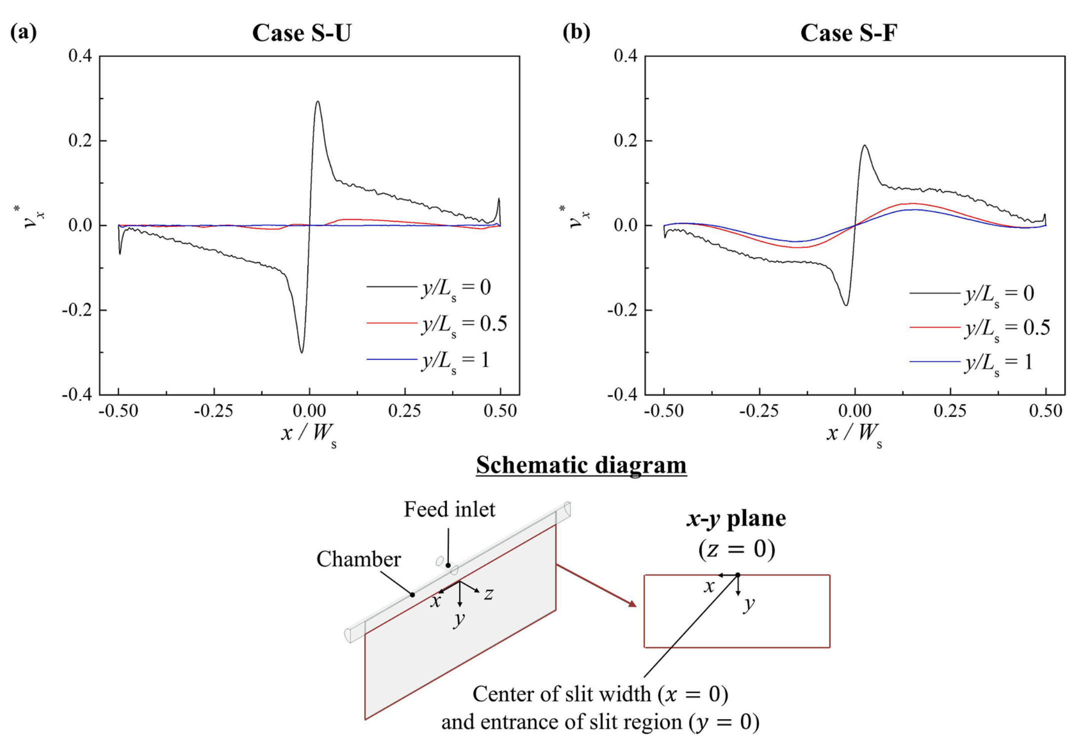

Fig. 9. Widthwise variations of the normalized x-velocity at various y-positions at the center of the slit height ($z = 0$) for (a) case S-U and (b) case S-F.

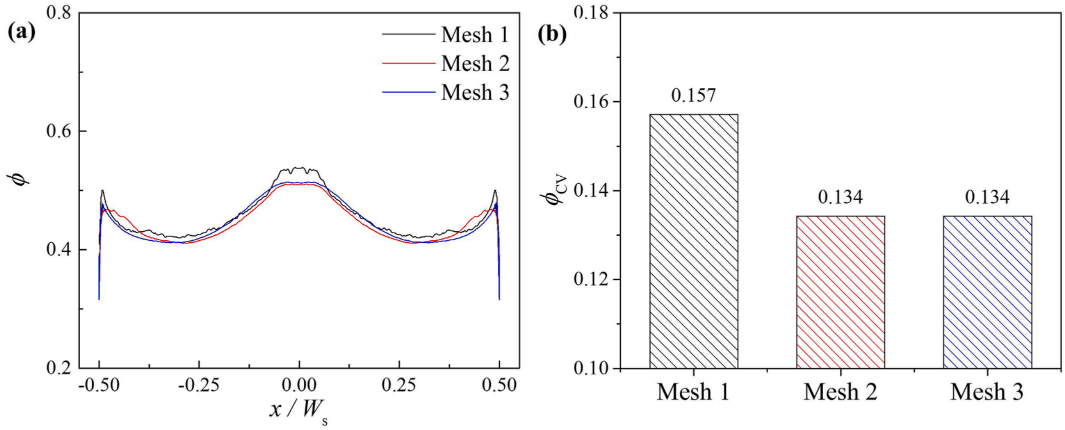

Fig. 10. Mesh convergence results; (a) widthwise profiles of particle volume fraction at the die exit ($z/H_s = +0.25$) for case S-F and (b) coefficient of variation of particle volume fraction (ϕ_{CV}) at the die exit across mesh elements.

demonstrating that particle concentration inhomogeneity at the slit entrance significantly delays flow development throughout the slit region.

3.2.4. Comparison between generalized Newtonian fluids and particulate suspensions

A comparison between the internal die flow results obtained for the aforementioned concentrated particulate suspensions and those obtained for particle-free generalized Newtonian fluids is instructive. Notably, the widthwise v^* profiles of cases S-F and C are non-uniform compared to case N and differ (Fig. 6(b) and 2(b)), whereas the gap-wise v^* profiles across the slit height exhibit similar trends, that is, blunt velocity profiles (Figs. 8 and 2(c)) at the die exit. These differences can be primarily attributed to particle advection ($\underline{v}\cdot\nabla\phi$) in case S-F. In case S-F, the dense particle concentration along the feed-inlet centerline was transported directly into the slit region along the streamlines, generating a locally elevated suspension viscosity near the center of the slit width. Consequently, lower v^* magnitudes appeared near the slit-width center in case S-F. In contrast, higher centerline v^* distributions in case C arose from the shear-thinning effect associated with the elevated effective shear rate near the center of the slit width.

3.2.5. Discussion on practical implications

Although direct experimental observations of particle distributions within the internal manifold are lacking, a previous experimental study reported a sudden decrease in wet thickness along the cross-web centerline, manifesting as a striped defect, during slot coating of lithium-ion battery slurries (Schmitt et al., 2013). The authors suggested that the striped defect could be caused by shear-induced agglomeration, which is qualitatively consistent with the inhomogeneous widthwise velocity profiles observed in case S-F.

These findings indicate that nonuniformity in the inlet particle distribution can significantly affect the internal die flow characteristics and retard flow development in the slit region. More in-depth analyses of the optimal die designs would require parametric studies in which the relevant parameters are systematically varied. However, such simulations require prohibitively long computation times for suspension cases. Based on the present analysis, rigorous theoretical investigations and advanced experimental studies are required to further elucidate particle migration phenomena in internal die flows.

4. Conclusion

This study investigated the effects of shear-induced particle migration on the internal die flow characteristics. Comparative three-dimensional CFD simulations demonstrated that particle migration markedly alters velocity uniformity at the die exit, as well as internal flow fields and particle distributions within the slot dies. Furthermore, the effects of inhomogeneous particle distributions generated at the feed inlet through long-supply pipelines were elucidated. The parabolic particle concentration profile at the feed inlet modified the flow dynamics within the chamber and significantly delayed flow development throughout the slit region.

Such nonuniform velocity and particle concentration profiles at the die exit can critically affect the operability window and promote flow instabilities in the coating bead region, ultimately leading to a nonuniform wet film thickness, including striped defects. Although a comprehensive parametric study of the optimal die design considering particle migration behaviors was not systematically performed because of prohibitive computational costs, the present results capture the essential features of shear-induced particle migration in internal die flows relevant to slot coating. These findings clarify the role of shear-induced particle migration in internal die flows and emphasize the need to control inlet particle concentration homogeneity to obtain uniform velocity and concentration profiles at the die exit. The resulting insights provide practical guidance for die design and process control to ensure a uniform coating thickness and stable slot coating operation in concentrated suspension systems.

CRediT authorship contribution statement

Min-Kyu Kim: Writing – review & editing, Writing – original draft, Methodology, Investigation, Formal analysis, Data curation, Conceptualization. **Hyun Wook Jung:** Writing – review & editing, Writing – original draft, Validation, Supervision, Methodology, Investigation, Funding acquisition, Conceptualization.

Declaration of competing interests

The authors declare that they have no known competing financial interests or personal relationships that could have appeared to influence the work reported in this paper.

Acknowledgment

This work was supported by the National Research Foundation of Korea (NRF) grants funded by the Ministry of Science and ICT (MSIT) of the Korea government (No. RS-2021-NR057526), and the Technology Innovation Program (No. RS-2024-00433401) funded by the Ministry of Trade, Industry, & Energy (MOTIE, Korea).

Appendix. Mesh convergence test

The computational mesh was optimized through a mesh convergence test to ensure that the numerical results are independent of mesh refinement. Fig. 10(a) presents the widthwise profiles of the particle volume fraction at the die exit ($z/H_s = +0.25$) for case S-F under different mesh configurations. For Mesh 1 (943,268 elements) and Mesh 2 (5,643,517 elements), the relative deviations in the maximum particle concentration are 4.7% and 0.7%, respectively, compared to Mesh 3 (9,529,747 elements).

Fig. 10(b) shows the coefficient of variation of the particle volume fraction (ϕ_{CV}) at the die exit across mesh elements. ϕ_{CV} is defined as follows:

$$\phi_{CV} = \left[\sum_{i=1}^{N} \frac{1}{N\langle\phi\rangle^2} (\phi_i - \langle\phi\rangle)^2 \right]^{1/2} \tag{14}$$

where N is the total number of sampling points, ϕ_i is the particle volume fraction at the i-th sampling point at the die exit, and $< \phi >$ denotes the average particle volume fraction over all sampling points. The value of ϕ_{CV} converges at Mesh 3. Therefore, Mesh 3 was adopted for all subsequent simulations in this study to ensure reliable numerical results.

References

Bajaj, M., Prakash, J. R., & Pasquali, M. (2008). A computational study of the effect of viscoelasticity on slot coating flow of dilute polymer solutions. *Journal of Non-newtonian Fluid Mechanics, 149*, 104–123. https://doi.org/10.1016/j.jnnfm.2007.05.013

Campana, D. M., Valdez Silva, L. D., & Carvalho, M. S. (2017). Slot coating flows of non-colloidal particle suspensions. *AIChE Journal, 63*, 1122–1131. https://doi.org/10.1002/aic.15444

Carvalho, M. S., & Kheshgi, H. S. (2000). Low-flow limit in slot coating: Theory and experiments. *AIChE Journal, 46*, 1907–1917. https://doi.org/10.1002/aic.690461003

Chun, B., Kwon, I., Jung, H. W., & Hyun, J. C. (2017). Lattice Boltzmann simulation of shear-induced particle migration in plane Couette-Poiseuille flow: Local ordering of suspension. *Physics of Fluids, 29*, Article 121605. https://doi.org/10.1063/1.4991428

Ding, X., Fuller, T. F., & Harris, T. A. (2013). Predicting fluid penetration during slot die coating onto porous substrates. *Chemical Engineering Science, 99*, 67–75. https://doi.org/10.1016/j.ces.2013.05.039

Ding, X., & Harris, T. A. (2017). Review on penetration and transport phenomena in porous media during slot die coating. *Journal of Polymer Science Part B: Polymer Physics, 55*, 1669–1680. https://doi.org/10.1002/polb.24307

Ding, X., Liu, J., & Harris, T. A. (2016). A review of the operating limits in slot die coating processes. *AIChE Journal, 62*, 2508–2524. https://doi.org/10.1002/aic.15268

Gates, I. D. (1999). *Slot coating flows: Feasibility, quality*. Ph.D. Thesis. United States: University of Minnesota.

Hampton, R., Mammoli, A., Graham, A., Tetlow, N., & Altobelli, S. (1997). Migration of particles undergoing pressure-driven flow in a circular conduit. *Journal of Rheology, 41*, 621–640. https://doi.org/10.1122/1.550863

Han, G. H., Lee, S. H., Ahn, W.-G., Nam, J., & Jung, H. W. (2014). Effect of shim configuration on flow dynamics and operability windows in stripe slot coating process. *Journal of Coatings Technology and Research, 11*, 19–29. https://doi.org/10.1007/s11998-013-9485-3

Higgins, B. G., & Scriven, L. E. (1980). Capillary pressure and viscous pressure drop set bounds on coating bead operability. *Chemical Engineering Science, 35*, 673–682. https://doi.org/10.1016/0009-2509(80)80018-2

Ji, H. S., Ahn, W.-G., Kwon, I., Nam, J., & Jung, H. W. (2016). Operability coating window of dual-layer slot coating process using viscocapillary model. *Chemical Engineering Science, 143*, 122–129. https://doi.org/10.1016/j.ces.2015.12.016

Jin, G. L., Ahn, W.-G., Kim, S. J., Nam, J., Jung, H. W., & Hyun, J. C. (2016). Effect of shim configuration on internal die flows for non-Newtonian coating liquids in slot coating process. *Korea-Australia Rheology Journal, 28*, 159–164. https://doi.org/10.1007/s13367-016-0015-6

Ju, S. H., Min, K., Kim, D., Nam, J., & Lee, J. M. (2026). Surrogate modeling of slot-die coating manifold for lithium-ion battery manufacturing using mode extraction methods. *Chemical Engineering Science, 320*, Article 122459. https://doi.org/10.1016/j.ces.2025.122459

Kim, M.-K., & Jung, H. W. (2025). Coating bead flows and operability windows of concentrated suspensions in slot coating processes considering shear-induced migration. *Journal of Plastic Film & Sheeting, 41*, 335–359. https://doi.org/10.1177/87560879251345838

Kim, M.-K., & Jung, H. W. (2026). Periodic particle concentration oscillations in slot coating of concentrated suspensions with shear-induced migration. *AIChE Journal, 72*, Article e70277. https://doi.org/10.1002/aic.70277

Kim, D., Song, H.-S., & Jung, H. W. (2025). Optimizing dual-shim configurations for Non-Newtonian coating liquids in the slot coating process of PEM fuel cells using artificial neural networks. *The European Physical Journal Special Topics, 234*, 1–12. https://doi.org/10.1140/epjs/s11734-024-01456-0

Kistler, S. F., & Schweizer, P. M. (1997). *Liquid film coating: Scientific principles and their technological implications*. Dordrecht: Springer. https://doi.org/10.1007/978-94-011-5342-3

Koh, H. J., Kwon, I., Jung, H. W., & Hyun, J. C. (2012). Operability window of slot coating using viscocapillary model for Carreau-type coating liquids. *Korea-Australia Rheology Journal, 24*, 137–141. https://doi.org/10.1007/s13367-012-0016-z

Krieger, I. M. (1972). Rheology of monodisperse latices. *Advances in Colloid and Interface Science, 3*, 111–136. https://doi.org/10.1016/0001-8686(72)80001-0

Kwon, I., Chun, M.-S., Chun, B., Jung, H. W., & Hyun, J. C. (2018). Particle migration in planar Couette–Poiseuille flows of concentrated suspensions. *Journal of Rheology, 62*, 419–435. https://doi.org/10.1122/1.4989416

Lee, Y. W., Ahn, W.-G., Nam, J., Jung, H. W., & Hyun, J. C. (2017). Operability windows in viscoelastic slot coating flows using a simplified viscoelastic-capillary model. *Rheologica Acta, 56*, 707–717. https://doi.org/10.1007/s00397-017-1026-z

Lee, K. Y., & Liu, T. J. (1989). Design and analysis of a dual-cavity coat-hanger die. *Polymer Engineering & Science, 29*, 1066–1075. https://doi.org/10.1002/pen.760291513

Lee, J., & Nam, J. (2016). A simple model for viscoplastic thin film formation for coating flows. *Journal of Non-newtonian Fluid Mechanics, 229*, 16–26. https://doi.org/10.1016/j.jnnfm.2015.12.012

Lee, M., Shin, K., & Nam, J. (2023). Operating limit of vacuum-assisted slot die coating of Herschel-Bulkley fluids. *Chemical Engineering Science, 274*, Article 118668. https://doi.org/10.1016/j.ces.2023.118668

Leonard, W. K. (1985). Inertia and gravitational effects in extrusion dies for non-newtonian fluids. *Polymer Engineering & Science, 25*, 570–576. https://doi.org/10.1002/pen.760250910

Matsubara, Y. (1979). Geometry design of a coat-hanger die with uniform flow rate and residence time across the die width. *Polymer Engineering & Science, 19*, 169–172. https://doi.org/10.1002/pen.760190302

McKelvey, J. M., & Ito, K. (1971). Uniformity of flow from sheeting dies. *Polymer Engineering & Science, 11*, 258–263. https://doi.org/10.1002/pen.760110314

Min, K. H., & Kim, C. (2010). Simulation of particle migration in free-surface flows. *AIChE Journal, 56*, 2539–2550. https://doi.org/10.1002/aic.12145

Nam, J., & Carvalho, M. S. (2009). Mid-gap invasion in two-layer slot coating. *Journal of Fluid Mechanics, 631*, 397–417. https://doi.org/10.1017/S0022112009007022

Nam, J., & Carvalho, M. S. (2010a). Flow in tensioned-web-over-slot die coating: Effect of die lip design. *Chemical Engineering Science, 65*, 3957–3971. https://doi.org/10.1016/j.ces.2010.03.032

Nam, J., & Carvalho, M. S. (2010b). Two-layer tensioned-web-over-slot die coating: Effect of operating conditions on coating window. *Chemical Engineering Science, 65*, 4065–4079. https://doi.org/10.1016/j.ces.2010.03.038

Nam, J., & Carvalho, M. S. (2010c). Linear stability analysis of two-layer rectilinear flow in slot coating. *AIChE Journal, 56*, 2503–2512. https://doi.org/10.1002/aic.12172

Nott, P. R., & Brady, J. F. (1994). Pressure-driven flow of suspensions: Simulation and theory. *Journal of Fluid Mechanics, 275*, 157–199. https://doi.org/10.1017/S0022112094002326

Park, J. S., Yoo, T., Chun, B., Lee, K.-Y., & Jung, H. W. (2022). Operability limits for Non-Newtonian liquids in dual-layer slot coating processes using the viscocapillary model. *Journal of Coatings Technology and Research, 19*, 35–47. https://doi.org/10.1007/s11998-021-00499-5

Phillips, R. J., Armstrong, R. C., Brown, R. A., Graham, A. L., & Abbott, J. R. (1992). A constitutive equation for concentrated suspensions that accounts for shear-induced particle migration. *Physics of Fluids A: Fluid Dynamics, 4*, 30–40. https://doi.org/10.1063/1.858498

Rebouças, R., Siqueira, I., & Carvalho, M. (2018). Slot coating flow of particle suspensions: Particle migration in shear sensitive liquids. *Journal of Non-newtonian Fluid Mechanics, 258*, 22–31. https://doi.org/10.1016/j.jnnfm.2018.04.007

Romero, O., Scriven, L., & Carvalho, M. (2006). Slot coating of mildly viscoelastic liquids. *Journal of Non-newtonian Fluid Mechanics, 138*, 63–75. https://doi.org/10.1016/j.jnnfm.2005.11.010

Romero, O., Suszynski, W., Scriven, L., & Carvalho, M. (2004). Low-flow limit in slot coating of dilute solutions of high molecular weight polymer. *Journal of Non-newtonian Fluid Mechanics, 118*, 137–156. https://doi.org/10.1016/j.jnnfm.2004.03.004

Sartor, L. (1990). *Slot coating: Fluid mechanics and die design*. Ph.D. Thesis. United States: University of Minnesota.

Schmitt, M., Baunach, M., Wengeler, L., Peters, K., Junges, P., Scharfer, P., & Schabel, W. (2013). Slot-die processing of lithium-ion battery electrodes—Coating window characterization. *Chemical Engineering and Processing: Process Intensification, 68*, 32–37. https://doi.org/10.1016/j.cep.2012.10.011

Schweizer, P. M. (2022). *Premetered coating methods: Attractiveness and limitations*. Cham: Springer. https://doi.org/10.1007/978-3-031-04180-8

Siqueira, I. R., & Carvalho, M. S. (2019). A computational study of the effect of particle migration on the low-flow limit in slot coating of particle suspensions. *Journal of Coatings Technology and Research, 16*, 1619–1628. https://doi.org/10.1007/s11998-019-00196-4

Siqueira, I. R., Rebouças, R. B., & Carvalho, M. S. (2017). Particle migration and alignment in slot coating flows of elongated particle suspensions. *AIChE Journal, 63*, 3187–3198. https://doi.org/10.1002/aic.15653

Siqueira, I. R., Thompson, R. L., Carvalho, M. S., & de Souza Mendes, P. R. (2024). Slot coating of viscoplastic materials: A computational study of the effects of viscoplasticity on the flow dynamics and low-flow limit. *Journal of Non-newtonian Fluid Mechanics, 327*, Article 105222. https://doi.org/10.1016/j.jnnfm.2024.105222